



# Ag–SiO<sub>2</sub>–TiO<sub>2</sub> nanocomposite coatings with enhanced photoactivity for self-cleaning application on building materials



Luís Pinho\*, María Rojas, Maria J. Mosquera\*

TEP-243 Nanomaterials Group, Departamento de Química-Física and IMEYMAT, Facultad de Ciencias, Universidad de Cádiz, Av. República Saharaui, 11510 Puerto Real, Cádiz, Spain

## ARTICLE INFO

### Article history:

Received 14 July 2014

Received in revised form

30 September 2014

Accepted 2 October 2014

Available online 17 October 2014

### Keywords:

Photocatalysis

Mesoporous Ag–SiO<sub>2</sub>–TiO<sub>2</sub> photocatalyst

Ag nanoparticles

Surface plasmon resonance

Self-cleaning

## ABSTRACT

The synthesis of improved photocatalysts capable of removing pollutants deposited on building surfaces is an important challenge for researchers nowadays. By using a simple and low-cost process we have synthesized mesoporous Ag–TiO<sub>2</sub>–SiO<sub>2</sub> photocatalytic coatings that meet the requirements of outdoor application. These are new materials designed to give to the building material improved self-cleaning properties.

We have varied the loading of TiO<sub>2</sub> and Ag nanoparticles in order to investigate their effect on the photocatalytic activity of our nanocomposites. We find that the integration of higher Ag loadings in a TiO<sub>2</sub>–SiO<sub>2</sub> network (10% w/w) significantly increase the photoactivity of the coating containing 1% (w/v) TiO<sub>2</sub> due to the improved absorption of visible light and higher surface area of the photocatalyst. For higher TiO<sub>2</sub> contents (4%) there is an increase in photoactivity for 1% (w/v) Ag loading. Higher amounts of Ag loadings (5% w/w) generate an undesired color change on stone or inhibit the sol–gel transition of the coatings (10% w/w).

© 2014 Elsevier B.V. All rights reserved.

## 1. Introduction

Scientists are nowadays facing major challenges in countering air pollution and specifically in devising ways of decomposing the organic species deposited on building surfaces, which are responsible for the deterioration of their appearance. Photocatalysts applied as coatings on buildings and stone structures can be an interesting solution in order to lower maintenance costs by reducing surface soiling and the need for costly cleaning operations [1].

Titanium dioxide is probably the most efficient common material with photocatalytic properties, very high stability, and very low cost. However, due to its wide bandgap, it can only absorb UV light, which represents a proportion of 4% of the complete solar spectrum. Therefore, the enhancement of the properties of TiO<sub>2</sub> photocatalyst coatings capable of absorbing visible light and of better removing pollutants is an important challenge for researchers nowadays.

Among the strategies available for enhancing visible light absorption on TiO<sub>2</sub>, noble-metal doping is especially pursued [2]. Among noble metals, Ag is a popular choice because of its high work function and of its ability to generate surface plasmons at desired wavelengths [3]. It is also well-known that silver nanoparticles are

chemically very reactive and would be oxidized at direct contact with TiO<sub>2</sub> [4]. In order to avoid the oxidation of Ag nanoparticles, in Ag–SiO<sub>2</sub>–TiO<sub>2</sub> photocatalysts, Ag nanoparticles can be coated with a material such as SiO<sub>2</sub> [4–9] or Al<sub>2</sub>O<sub>3</sub> [10] which acts as an interlayer in order to avoid the oxidation of silver and to modulate the distance between silver and the TiO<sub>2</sub> semiconductor [4].

At the present moment, few attempts to apply noble-metal/TiO<sub>2</sub> photocatalysts that are able to absorb solar light on building surfaces, have been reported in the literature. In this regard, Bergamonti et al. [11] have applied Au–TiO<sub>2</sub> dispersions and have been successful in obtaining higher photoactivity with these materials. Several other references can be found in the literature concerning the employment of water dispersions of TiO<sub>2</sub> particles [12] or of commercial products consisting of an aqueous dispersion with TiO<sub>2</sub> and an acrylic polymer on building surfaces [13].

However, the application of such strategies cannot ensure the long-term performance of the coating because TiO<sub>2</sub> particles deposited on the surface can easily be removed from external porous building surfaces [14]. One strategy for preventing the release of the TiO<sub>2</sub> from the surface to the environment would be to immobilize the photocatalyst in, for example, a SiO<sub>2</sub> matrix [15–17].

In order to avoid this inconvenience, we have previously developed synthesis routes in which TiO<sub>2</sub> crystalline nanoparticles are included in silica sol and applied in situ, as sols that penetrate and gel into the pores of building substrates, by using a simple process.

\* Corresponding authors. Tel.: +34 956016490/95601631; fax: +34 956016288.  
E-mail addresses: [luis.pinho@uca.es](mailto:luis.pinho@uca.es) (L. Pinho), [mariajesus.mosquera@uca.es](mailto:mariajesus.mosquera@uca.es) (M.J. Mosquera).

They finally generate mesoporous coatings without the need of performing post-synthesis treatments such as calcination or solvent extraction [18].

In addition, we have recently designed several syntheses of superhydrophobic [19] and stain-resistant [20] products intended to protect building materials, which meet the same requirements for application on building surfaces. Some of these products are now commercially available under the corresponding exploitation patents [21,22].

In the specific case of the self-cleaning product devised, an Ag-SiO<sub>2</sub>-TiO<sub>2</sub> nanocomposite coating gives photocatalytic properties to stone surfaces. This product also penetrates into the pore structure of the stone, increasing its robustness. It consists of a colloidal dispersion of TiO<sub>2</sub> and Ag nanoparticles included in a sol of silica oligomers, in presence of a surfactant (*n*-octylamine), which can be applied to building materials by means of an aerosol-assisted process. The surfactant acts to coarsen the pore structure of the gel network generating an enhancement of photocatalytic activity by creating a mesoporous nanocomposite. It also helps to prevent cracking, to improve the dispersion of TiO<sub>2</sub> and Ag nanoparticles and to catalyze sol-transition of the nanocomposites applied.

Since the microstructural, textural and optical parameters of Ag-SiO<sub>2</sub>-TiO<sub>2</sub> nanomaterials play an important role in their performance as photocatalysts the first objective of the work reported here is to investigate their in the properties of photocatalysts. This has been done by integrating TiO<sub>2</sub> and Ag nanoparticles into a SiO<sub>2</sub> matrix. To achieve this objective, we investigate the structure of these materials in depth using several techniques including N<sub>2</sub> physisorption, SEM, TEM, and UV-vis spectroscopy.

Our second objective is to understand the performance of these Ag-SiO<sub>2</sub>-TiO<sub>2</sub> photocatalysts on stone. Thus, we apply the materials synthesized in our laboratory on a pure limestone employed in both modern and ancient buildings, and evaluate the performance of the products for photocatalytic activity and adhesion on the stone surface. In addition, we also evaluate the hydrophobic properties and the color change generated by these photocatalysts on stone, in order to understand their ability to meet the requirements associated with protective coatings for stonework.

## 2. Experimental

### 2.1. Synthesis

The following reagents were used in the synthesis process: (1) TES40 WN (Wacker Chemie AG, GmbH): according to the technical data sheet, this is an ethoxysilane (average polymerization grade of 5) providing approximately 41% of silica upon complete hydrolysis and many hydrolysable ethoxy groups; (2) *n*-octylamine (Aldrich); (3) AgNO<sub>3</sub> (Panreac), (4) commercial colloidal VP TiO<sub>2</sub> nanoparticles, with an average particle size of 20 μm, surface area of 50 ± 15 and pH in dispersion of 3.0–4.5. The N<sub>2</sub> adsorption-desorption isotherms (Fig. S1) and the XRD spectra (Fig. S2) of these nanoparticles can also be observed in Supplementary Information. Syntheses were carried out as follows: TES40 was mixed with TiO<sub>2</sub> nanoparticles in the presence of *n*-octylamine under high-power ultrasonic agitation (125 W cm<sup>-3</sup>). The proportion of *n*-octylamine to TES40 was 0.36% v/v. Next, TiO<sub>2</sub> nanoparticles and 1 mol/l aqueous solution of AgNO<sub>3</sub> was also added to each formulation. A set of formulations was prepared for each kind of particle tested. These were designated S#Ti§Ag where # indicates the % (w/v) of VP TiO<sub>2</sub> nanoparticles included in the material (i.e. the loading). The symbol § indicates the % (w/w) of Ag present in the material with respect to TiO<sub>2</sub>. TiO<sub>2</sub> nanoparticles were added to the starting sol in two different proportions: 1, 4% (w/v). AgNO<sub>3</sub> was added in three different proportions: 1, 5 and 10% (w/w). For

comparative purposes, Ag-SiO<sub>2</sub> materials without TiO<sub>2</sub> nanoparticles (designated S§Ag(#)) and a pure silica material (SOTAg) were also prepared according to the same synthesis.

Supplementary Figs. S1 and S2 related to this article can be found, in the online version, at <http://dx.doi.org/10.1016/j.apcatb.2014.10.002>.

### 2.2. Sol-gel characterization

Immediately after the synthesis of the sols, their rheological properties were studied using a concentric cylinder viscosimeter (model DV-II+ with UL/Y adapter) from Brookfield. Experiments were performed at a constant temperature of 25 °C maintained by recirculated water from a thermostatic bath. A shear stress versus shear rate flow curve was generated. For comparison, the rheological properties of TES 40 were also evaluated. We have also obtained UV-vis absorption spectra of our sols in order to investigate the formation of silver species. This study was carried out by using an ATI Unicam UV4 spectrophotometer.

Next, coatings of the materials under study were obtained by deposition of 3 ml of sol on plastic Petri dishes with a diameter of 85 mm. Dishes were covered and maintained at laboratory conditions (relative humidity of 60% and temperature of 20 °C). Gel transition and spontaneous drying took place. The xerogels obtained were characterized after reaching constant weight.

Powdered VP nanoparticles were used for X-ray diffraction (XRD), measured on a Bruker D8 advance diffractometer equipped with a secondary monochromator, Cu tube X-ray, using Cu K<sub>α</sub> radiation. The photocatalyst coatings were visualized by scanning electron microscopy (SEM) using a FEI Sirion instrument with a field emission filament operating at 5 kV. This instrument has a resolution of 1.5 nm and it is equipped with a Through-Lens Detector (TLD) working in ultra-high resolution (UHR) mode.

Textural characterization was performed by N<sub>2</sub> physisorption at 77 K, using a Quantachrome Autosorb IQ. The isotherms obtained were used to calculate pore volume and surface area of the powdered nanomaterials. The adsorption data were analyzed using a hybrid NLDFT (non-local density functional theory) approach that allows quantification of both micro- and mesopores in order to obtain the pore size distribution of materials containing pores of different geometry [23].

Transmission electron microscopy studies were performed in a JEOL 2010F TEM/STEM microscope, operating at 200 kV with 0.19 nm spatial resolution. This instrument is equipped with a JEOL high angle annular dark field (HAADF) detector, enabling the acquisition of STEM images. Samples were prepared by depositing a small amount of the powders directly onto Lacey-carbon coated Cu grids. Both TEM and HAADF images were obtained. It is also important to refer that HAADF detectors capture electrons that undergo high angle scattering and the signal is approximately proportional to Z<sup>2</sup>, where Z is the atomic number. They provide contrast sensitive to compositional changes, and allow the identification of components with different atomic numbers in nanocomposite materials [24].

Diffusive reflectance UV-vis spectra of the photocatalysts were recorded on a Shimadzu UV-3100 spectrometer with an integrating sphere attachment using BaSO<sub>4</sub> powder as white reference. The band-gap of our photocatalysts was calculated by using the Kubelka-Munk functions according to the method proposed by Tandon and Gupta [25].

Single-pulse (SP) MAS-NMR experiments were carried out on a Bruker ADVANCE WB400 spectrometer equipped with a multi-nuclear probe. Samples of powdered materials were packed in 4 mm zirconia rotors and spun at 8 kHz. <sup>29</sup>Si MAS NMR spectra were acquired at a frequency of 79.49 MHz, using a pulse width of 1.8 μs (π/2 pulse length = 5.4 μs), a delay time of 60 s and scan

number of 2000. The chemical shift values are reported in ppm from tetramethylsilane.

### 2.3. Application on stone and characterization

The stone selected for evaluating the effectiveness of the materials under study is a limestone with a homogeneous structure, composed of a micritic matrix containing oolites and oncolites, and it is mainly composed of calcite (100%). This stone was selected for its whiteness, so the stains applied on its surface and the self-cleaning effectiveness of the coatings under study could be checked more easily. For all the experiments carried out, the stone samples were cut in the form of  $5\text{ cm} \times 5\text{ cm} \times 2\text{ cm}$  slabs. The sols under study were applied by spraying onto the surfaces of the samples until apparent refusal, this being understood to occur when the surfaces remained wet for 1 min. After the application, the excess of sol was removed from the surface of the sample by air spraying, in order to form the thinnest possible surface film [26]. The stone samples were then dried under laboratory conditions until reaching constant weight. Uptake of products and their corresponding dry matter were calculated. The samples corresponding to untreated stone and their treated counterparts were characterized by the procedures described below, after constant weight was reached. All the results reported correspond to average values obtained from three stone samples.

The adherence of the coating to the stone surface was evaluated by performing a peeling test using Scotch® Magic™ tape (3 M). The test was carried out according to previously reported methods [27].

Changes in water absorption after treatments were evaluated by applying a test of capillary water absorption, as recommended in UNE-EN 1925 [28]. Total water uptake (TWU) values obtained after 48 h were determined.

We also evaluated the possible disadvantage of these materials associated with changes in stone color induced by the treatments. This effect was determined using a solid reflection spectrophotometer, Colorflex model, from Hunterlab. The conditions used were: illuminant C and observer 2°. CIELa\*b\* color space was used and variations in color were evaluated using the parameter: total color difference ( $\Delta E^*$ ) [29].

The effectiveness of the materials under study as self-cleaning coatings for stone surfaces was evaluated by using a test adapted from the literature [30]. First, 1 ml of a solution of 1 mM methylene blue (Panreac) in ethanol was deposited on treated stone specimens and their untreated counterparts. Next, stone samples were irradiated with UV light working at 365 nm in a Vilber Lourmat CN15.CL chamber with 2 tubes of 15 W. The distance between the samples and the tubes was approximately 20 cm. Color variations, recorded as a function of irradiation time, were determined using the same procedure described above. The parameter: total color difference ( $\Delta E^*$ ) was again evaluated [29] and the photocatalytic activity is expressed as  $\% \Delta E^*$ .  $\% \Delta E^*$  is given by the following expression:  $100 - (((\Delta E^* - \Delta E^*_0) / \Delta E^*_0) \times 100)$ , where  $\Delta E^*_0$  is the value obtained for the total color difference between the stained and unstained samples at the beginning of the test ( $t = 0\text{ h}$ ).  $\Delta E^*$  corresponds to the same measurements recorded at each irradiation time.

## 3. Results and discussion

### 3.1. Sol–gel characterization

Our photocatalysts are prepared in a one-step synthesis and applied as aerosols at ambient temperature on porous substrates. Therefore, the rheological properties of our sols are a key factor for facilitating their application and for predicting their in-depth

distribution on porous substrates. We have carried out viscosity measurements of the synthesized sols immediately after ultrasonic stirring of the dispersions. Table 1 presents the viscosity values obtained for the sols under study. The viscosity of the silica precursor employed in the syntheses (TES 40) was also evaluated for comparison purposes. Since the behavior shown by the prepared sols was always nearly Newtonian at the shear range evaluated, viscosity was calculated as the slope of the shear rate vs. shear stress curves. Linear regression coefficients of 0.99 were obtained in the most of the cases.

The viscosity values obtained for S0T0Ag and for the S1T\*Ag series were very similar to those corresponding to commercial silica sols employed on stones and other building materials. Specifically, we determined the viscosity for one of the most popular commercial stone consolidants, Tegovakon V100 from Evonik; the viscosity of this solvent-free product was 5.25 mPa s at 25 °C [31]. As a result, we conclude that the sols prepared in our laboratory must ensure an adequate penetration into the porous building substrates.

Three main trends can be observed in the rheology of the sols under study. Firstly, by comparing the viscosity values obtained for TES40 and S0T0Ag there is a slight increase when *n*-octylamine is added to TES40. This can be explained by the initial effect of *n*-octylamine as a sol–gel catalyst.

Secondly, an increase of TiO<sub>2</sub> particle loading produces an increase in the values of viscosity. However, the loading of 1% does not significantly modify the rheological behavior of the S0T§Ag sols. In the case of S4T§Ag sols, we have previously explained the increase in viscosity values in terms of the increase of TiO<sub>2</sub> particle concentration [17].

Finally, in the case of the Ag–SiO<sub>2</sub>–TiO<sub>2</sub> sols under study, the addition of an aqueous solution of AgNO<sub>3</sub> produced a decrease in viscosity values. This trend can be observed both for S1T§Ag and S4T§Ag sols which contain increasing amounts of water and silver ions, which are added simultaneously to the sol in the AgNO<sub>3</sub> aqueous solution (Table 1). We hypothesize that this decrease of viscosity values in the early stage formation of our sols is mainly due to the increase amount of water, which does not seem to be increasing the hydrolysis rate of our sols. In a similar way, a decrease of viscosity for increasing amounts of water in silica sols has been previously obtained by Wu et al. [32]. The effect of the addition of silver ions has additional implications in the properties of our nanocomposites and will be discussed in later paragraphs of this discussion.

Regarding the stability of our dispersions during the sol–gel transition, we have previously discussed it in terms of an increase in the pH values of the sol, produced by *n*-octylamine, which is responsible for enhancing electrostatic repulsions and the stability of TiO<sub>2</sub> nanoparticles [17]. The addition of the AgNO<sub>3</sub> aqueous solution to the sol does not significantly modify the stability of the dispersions generated by the presence of *n*-octylamine. Other amines or amine-terminated groups are reported to stabilize Ag dispersions and to avoid aggregation in silica sols [33–35].

The sol–gel transition of the sols deposited on plastic Petri dishes took place overnight, producing homogeneous composite gels, except for the S4T10Ag formulation, in which sol–gel transition did not occur. We explain this in terms of two related phenomena. Firstly, we hypothesize that when the amount of TiO<sub>2</sub> and Ag nanoparticles in the sol is maximum (S4T10Ag sol), *n*-octylamine interacts with the highest number of TiO<sub>2</sub> and Ag nanoparticles to stabilize them in dispersion. Secondly, besides enhancing the dispersion of Ag nanoparticles in silica sols, primary amines [34], aminosilanes [35] and aminoacids [7] are also reported to act as reducing agents of Ag species. Ethanol, which is generated as a product of the hydrolysis reaction of the silica precursor could act in a similar way to reduce Ag species [36].

**Table 1**

Viscosity, textural parameters and  $E_g$  obtained for the nanocomposites under study. Textural parameters were calculated by applying the NLDFT approach to the respective adsorption isotherms.

Product series	Viscosity (mPa s)	$S_{\text{total}}$ (m <sup>2</sup> /g)	$V_{\text{pore}}$ (cm <sup>3</sup> /g)	Pore size (mode) (nm)	$E_g$ (eV)
TES40	4.82	–	–	–	–
S0T0Ag	5.09	231	0.39	6.3	–
S1T0Ag	5.99	124	0.22	6.9	3.59
S1T1Ag	5.45	435	0.58	5.4	3.49
S1T5Ag	5.32	438	0.73	6.7	3.25
S1T10Ag	4.31	659	0.76	4.6	2.82
S4T0Ag	10.4	396	0.49	4.9	3.40
S4T1Ag	8.55	225	0.44	6.7	3.29
S4T5Ag	6.91	97	0.36	16	3.24
S4T10Ag	5.66	–	–	–	–

Thus, the concomitant roles of stabilization and reduction of Ag species played by *n*-octylamine in the sol would prevent it from acting effectively as a sol–gel catalyst, inhibiting the sol–gel transition for S4T10Ag. This hypothesis is supported by the occurrence of sol–gel transition in the sols with lower Ag amounts added during the synthesis.

In order to confirm the formation of silver nanoparticles in our sols, we have studied their optical behavior by using UV–vis spectroscopy. Fig. 1 shows typical UV–vis spectra of our sols after ultrasonic stirring and corresponding to the formulation S10Ag(1). These spectra were obtained at increasing times, up to 120 min, and show the progressive formation of a strong and broad band localized surface plasmon resonance (LSPR) absorption band and its redshift from around 500 nm to 570 nm. This indicates that silver nanoparticles are formed in our silica sol, probably due to the reduction of Ag<sup>+</sup> ions to Ag in presence of *n*-octylamine. Moreover, as Jiang et al. [9] have previously reported, this absorption behavior is due to the collective absorption behavior of Ag nanoparticles with quadrupole or higher resonances due to the strong interaction between nanoparticles. The formulations containing TiO<sub>2</sub> could not be analyzed with this method, since the addition of this component to the sol prevents the transmission of the UV–vis beam through the liquid sample. The formulations including TiO<sub>2</sub> and Ag are also expected to behave similarly to S10Ag(1). Finally, we have confirmed that the behavior of all the S $\#$ Ag(1) formulations was similar to the one presented by S10Ag(1).

Fig. 2 shows SEM micrographs of the Ag–SiO<sub>2</sub>–TiO<sub>2</sub> nanocomposites under study. S and S $\#$ T0Ag materials have also been examined for comparison purposes. All the materials form a homogeneous and continuous gel coating composed of aggregates visible at the magnification employed. Some differences can be observed with respect to the size of the aggregates comprising the gel network

of the different nanocomposites under study. The S0T0Ag material consisted of a configuration of silica nanoparticles of nearly uniform pore size. This particulate material presents a smaller and more homogeneous particle size (around 90 nm) that those corresponding to any materials including TiO<sub>2</sub> or both TiO<sub>2</sub> and Ag.

Silica nanomaterials with similar structures have been obtained by other authors in the presence of *n*-octylamine [37] or ammonia [38]. In this context, Bogush and Zukoski [38] developed an aggregative growth model to explain the formation of uniform silica nanoparticles in a basic medium, such as ammonia, in which the rate of condensation is faster than the hydrolysis. In our materials, we also speculate that the formation of silica nanoparticles occurs by a similar aggregation mechanism, which takes place due to the role played by *n*-octylamine as a basic catalyst, promoting the condensation of silica oligomers present in the starting sol [39].

Regarding the effect of TiO<sub>2</sub> loading on the aggregate size (Fig. 2), higher loadings cause a clear increase in the average particle size of the aggregates (110 nm for S1T0Ag and 150 nm for S4T0Ag) due to the presence of TiO<sub>2</sub> nanoparticles mixed with those of SiO<sub>2</sub>. This can be explained as a consequence of the larger size of the pre-formed TiO<sub>2</sub> nanoparticles employed in this study in comparison to the silica particles created during sol–gel transition. It is also important to remark that the initial 20  $\mu$ m size of VP nanoparticles indicated by the manufacturer is reduced from a micrometer to a nanometer scale, due to the strong cavitation power of ultrasonic stirring, as we previously discussed [17].

Considering the effect produced by the addition of aqueous Ag species to our nanocomposites, Two different tendencies can be observed. First, with respect to the lowest TiO<sub>2</sub> loading, we observe a decrease in particle size for lower amounts of Ag. Specifically, the images corresponding to S1T1Ag and S1T5Ag present aggregates with an approximate size of 50 and 75 nm, respectively. We explain this decrease in the size of the aggregates in terms of the small amount of Ag species present in the material. In these two cases, the water added to the sols is responsible for improving the hydrolysis of the silica precursors during all the sol–gel transition (approximately 12 h) and also for facilitating the formation of well-condensed particles in presence of the *n*-octylamine catalyst. However, when higher amounts of Ag are included in the nanocomposite, little differences can be found between the size of the aggregates present in S1T10Ag and S1T0Ag.

Second, when higher TiO<sub>2</sub> contents 4% are considered, the addition of Ag species to the material generates an increase of the average size of the aggregates, up to 150 and 200 nm, in the case of S4T1Ag and S4T5Ag, respectively.

We attribute the increase in the size of the aggregates to the previously reported interactions of *n*-octylamine with TiO<sub>2</sub> [40], and of *n*-octylamine with Ag [33], which may have an important influence in the process of formation of aggregates. If some of the surfactant is adsorbed on the surface of TiO<sub>2</sub> and Ag particles, less *n*-octylamine is available to catalyze the sol–gel transition when their respective loadings are raised. We have previously observed this

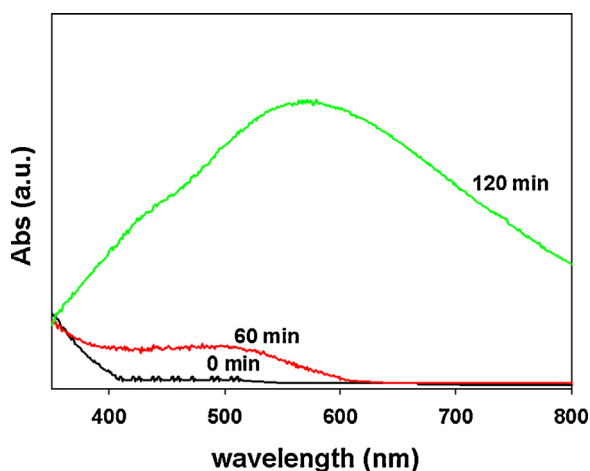


Fig. 1. Evolution of the UV–vis spectra of the sol S10Ag(1) with time.



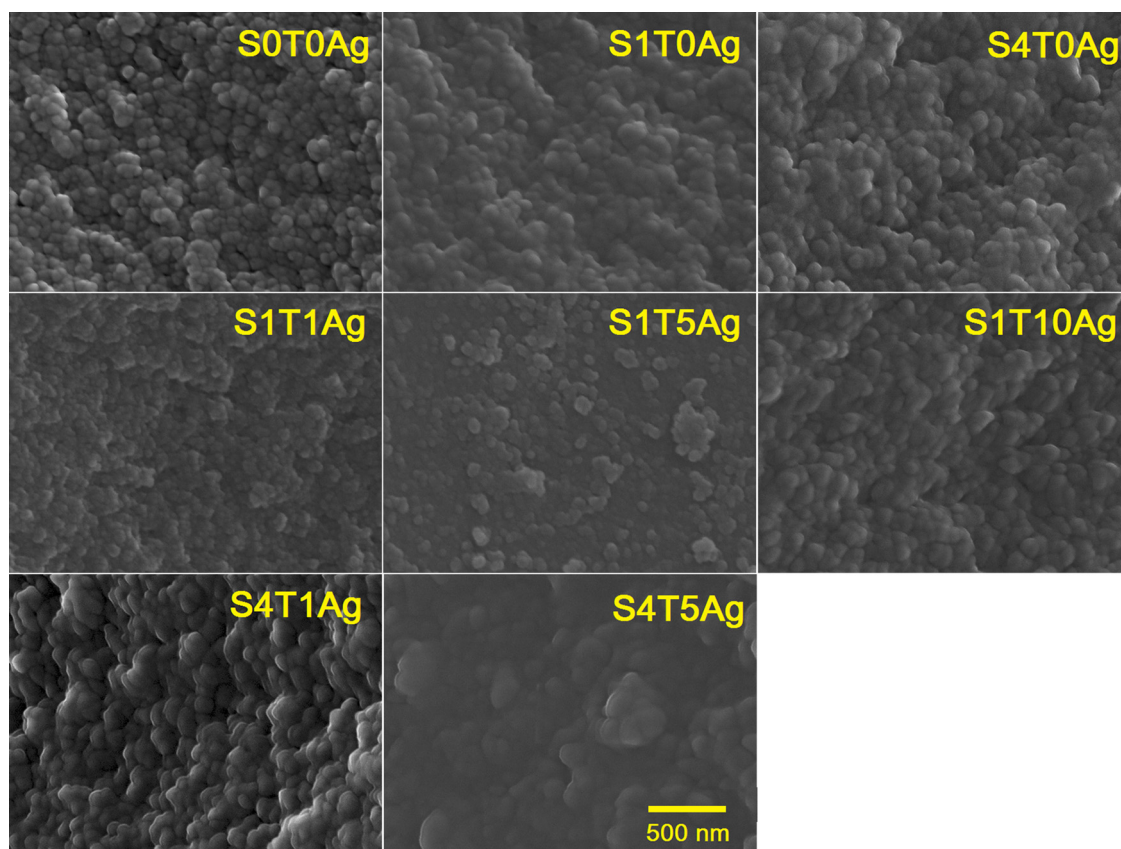


Fig. 2. SEM images of the photocatalysts under study.

suppressive effect of the silica condensation according to the proposed aggregation mechanism [17]. This possibility is confirmed by the appearance of the nanocomposites, which is more rigid for the materials with lower  $\text{TiO}_2$  and Ag loadings. Before, we have associated these differences with a higher degree of silica condensation in these materials [17].

In order to investigate in more depth the porous structure of these materials,  $\text{N}_2$  physisorption tests were carried out. Adsorption–desorption isotherms and NLDFT pore size distributions obtained from the isotherm adsorption branches for the materials under study are shown in Fig. 3. We have also included the pore size distribution on S1T0Ag in Fig. S3 in Supplementary Information) due to overlapping between the different representations of the pore size distribution. The textural data obtained are given in Table 1. VP  $\text{TiO}_2$  nanoparticles, were also characterized for comparative purposes (see Fig. S1 in Supplementary information). These nanoparticles present a type IV isotherm with a H1 hysteresis loop, as expected for an agglomerate of  $\text{TiO}_2$  nanoparticles [41].

Considering the nanocomposites synthesized in our laboratory, all the materials, including S (with no  $\text{TiO}_2$  and no Ag) show type IV isotherms as a consequence of the coarsening effect on the gel network exerted by *n*-octylamine [18]. Regarding hysteresis, most of the materials present a triangular hysteresis loop, classified as an H2 loop. However, a progressive change from a H2 to a H1-shaped loop (characterized by parallel and nearly vertical branches) occurs when the amounts of Ag present in the nanocomposites are increased. These changes in the texture of our nanocomposites are supported by the information provided in SEM images obtained for S1T10Ag and S4T5Ag materials (Fig. 2), which present the largest aggregates in its corresponding series of  $\text{TiO}_2$  loading (1 and 4%, respectively). According to the literature these materials could consist of spherical particles with high uniformity of pore size and high connectivity between pores [41]. Materials with H2

hysteresis present a similar structure but with lower connectivity. These isotherm profiles therefore suggest that all our materials are composed of a network of silica spheres, and the  $\text{TiO}_2$  and Ag particles are integrated within this network. We have previously obtained similar morphologies [18], consisting of a dispersion of  $\text{TiO}_2$  nanoparticles inside a regular matrix of uniform silica spheres. These results also confirm the aggregation mechanism previously proposed.

Some important differences between our materials are also observed in the  $\text{TiO}_2$  loading effect on their texture (Table 1). For  $\text{TiO}_2$  loading rates of 1% (S1T0Ag), the materials show a decrease in surface area and pore volume. For 4%  $\text{TiO}_2$  loadings (S4T0Ag), there is a significant increase in the values corresponding to both parameters, with respect to the pure silica material (S0T0Ag). This inverse relationship can be explained as a consequence of a higher proportion of non-porous  $\text{TiO}_2$  nanoparticles being incorporated in a coarser and worse-packed  $\text{TiO}_2$ – $\text{SiO}_2$  gel network for S4T0Ag.

Higher Ag loadings generate a progressive increase in surface area and pore volume for S1T%Ag photocatalysts and the opposite effect is observed for S4T%Ag. These variations correspond well to the increase and the decrease in the size of the aggregates observe for S1T%Ag and S4T%Ag, respectively. Considering NLDFT pore size distributions (Fig. 3 and Fig. S3 in Supplementary Information), we observe their displacement to lower values and a narrowing effect for all the photocatalysts evaluated, with respect to S0T0Ag.

Supplementary Fig. S3 related to this article can be found, in the online version, at <http://dx.doi.org/10.1016/j.apcatb.2014.10.002>.

In previous studies, the increase of Ag loading in similar Ag– $\text{SiO}_2$ – $\text{TiO}_2$  systems is reported to generate a decrease [7,42] or only a slight increase [5] in the surface area of the final materials. As we have previously discussed, the use of pre-formed  $\text{TiO}_2$  nanoparticles acts to open the  $\text{SiO}_2$  framework, generating voids between the aggregates [17]. In addition, our one-step synthesis method ensures

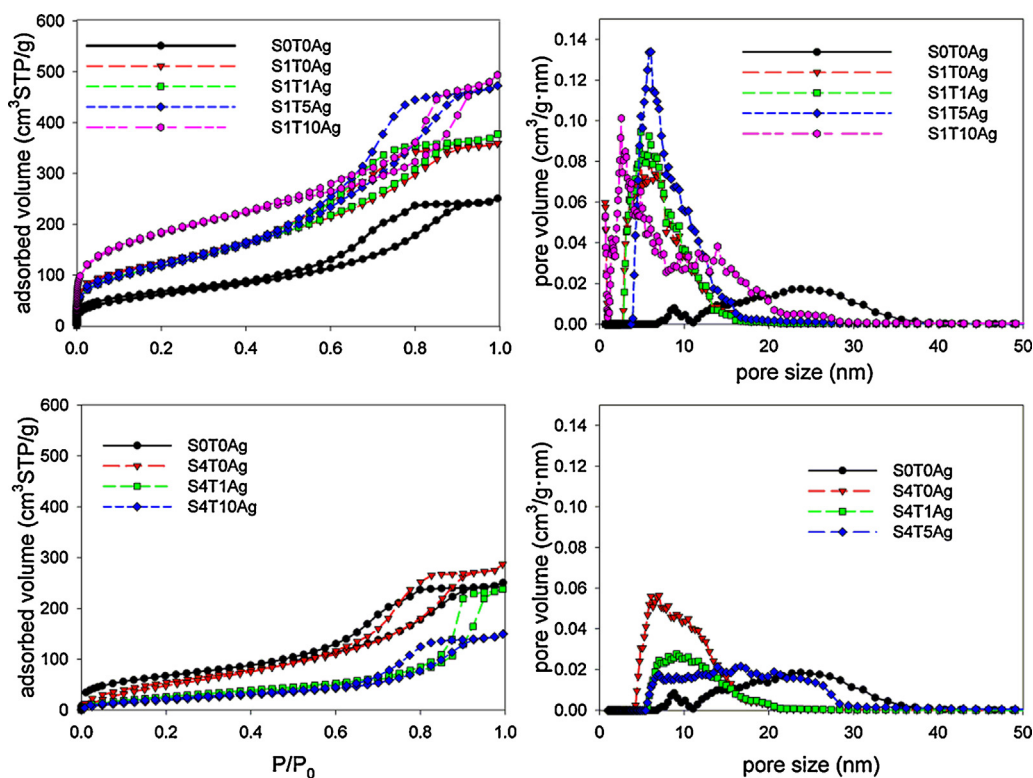


Fig. 3. Isotherms and NLDFT pore size distributions obtained for the photocatalysts under study.

that Ag nanoparticles are integrated in the structure of the material from the very early stage of its formation. By avoiding additional deposition treatments, we also ensure that Ag nanoparticles do not fill the voids created during the gelation and drying processes.

For a deeper investigation of the distribution of Ag, TiO<sub>2</sub> and SiO<sub>2</sub> in our photocatalysts materials, we carried out a transmission electronic microscopy (TEM) study. Fig. 4 shows representative images of the S1T10Ag material acquired in TEM (4a) and HAADF-STEM (4b) modes. This photocatalyst was selected for this detailed structural study on the basis of its efficient photocatalytic behavior and the good dispersion of Ag domains, as will be discussed later.

In Fig. 4a, three important features of our nanocomposites: (1) the existence of three clearly distinct and separate domains corresponding to a SiO<sub>2</sub> mesoporous matrix where individual TiO<sub>2</sub> and Ag nanoparticles are included; (2) differences in size and electron-density contrast of TiO<sub>2</sub> and Ag nanoparticles are clearly visible

in the images. (3) TiO<sub>2</sub> presents a crystalline configuration due to the visible lattice spacing present in the structure of the material, whereas SiO<sub>2</sub> presents an amorphous configuration in the absence of this lattice spacing; in the case of Ag domains, the lattice spacing is more difficult to observe, due to their reduced size and overlapping of TiO<sub>2</sub> and Ag. For the same reasons, our numerous attempts to obtain bidimensional high resolution images and the corresponding digital diffraction patterns of Ag nanoparticles were always unsuccessful.

The STEM-HAADF image obtained for S1T10Ag (Fig. 4b) shows individual TiO<sub>2</sub> and Ag domains (Ag appears brighter than TiO<sub>2</sub>) of different sizes inside the SiO<sub>2</sub> mesostructure. These images are particularly valuable for providing better insight into the SiO<sub>2</sub> porous network (which appears less bright than TiO<sub>2</sub> and Ag in the image), and allowing us to confirm the particle sizes obtained for Ag, TiO<sub>2</sub> and SiO<sub>2</sub> obtained in TEM images. From these images, additional

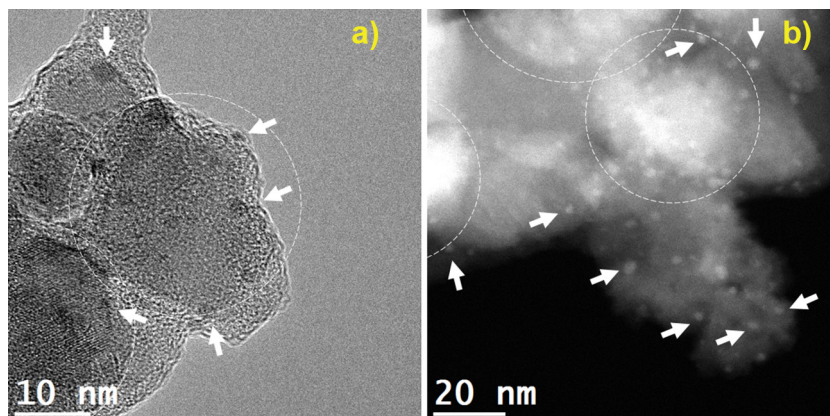


Fig. 4. Representative TEM (a) and STEM-HAADF (b) images obtained for the photocatalyst S1T10Ag. TiO<sub>2</sub> domains and Ag nanoparticles are signaled with dashed circles and with arrows, respectively.

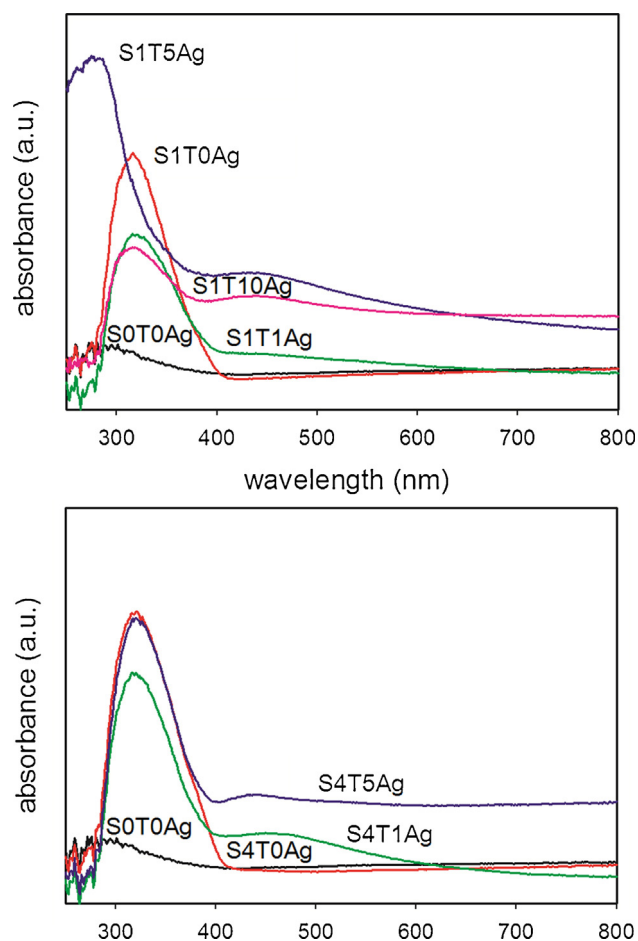


Fig. 5. UV-vis diffuse reflectance spectra of the photocatalysts under study.

features can be established for our materials. Firstly, the disaggregation produced by ultrasound stirring resulted in the presence, of  $\text{TiO}_2$  nanoparticles with an elongated particle shape and with a particle size of around 40–50 nm [17]. Smaller Ag nanoparticles, with spherical shape and particle sizes between 2 and 5 nm are also present in our nanocomposites. X-EDS spectra corresponding to the two types of particles integrated in the  $\text{SiO}_2$  matrix of our nanocomposites can be found in Supplementary Information (Fig. S4).

Supplementary Fig. S4 related to this article can be found, in the online version, at <http://dx.doi.org/10.1016/j.apcatb.2014.10.002>.

Secondly, the brighter Ag nanoparticles present a good dispersion along the  $\text{SiO}_2$  matrix, which has been previously reported to be beneficial for electron transfer from Ag to the conduction band of  $\text{TiO}_2$  [7]. All the other materials containing Ag showed worse dispersions and a larger particle size for Ag nanoparticles.

Thirdly, the dispersed Ag nanoparticles are preferentially integrated in the  $\text{SiO}_2$  matrix, which acts an insulating interlayer between  $\text{TiO}_2$  and Ag. Such an interlayer can prevent direct electron transfer between Ag and  $\text{TiO}_2$ , increasing the stability of Ag, and to adjust the coupling between the LSPR of Ag and  $\text{TiO}_2$  and to modulate the photocatalytic efficiency [3,9,10].

The diffuse reflectance UV-vis spectra obtained for all the photocatalysts are shown in Fig. 5, with the object of evaluating the absorption range of our photocatalysts. The Tauc plots used for the bandgap calculation (Table 1) can be analyzed in Fig. S5, Supplementary Information. In Fig. 5, we can observe that all the photocatalysts show absorption in the UV range (up to 400 nm). The pure silica material (S0T0Ag), together with the  $\text{TiO}_2$ -loaded

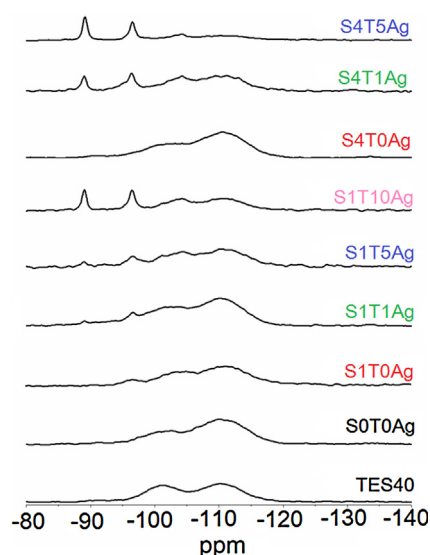


Fig. 6.  $^{29}\text{Si}$  NMR spectra of the photocatalysts under study.

photocatalysts (S1T0Ag and S4T0Ag) do not show absorption in the visible range. This indicates that the inclusion of  $\text{TiO}_2$  nanoparticles in a  $\text{SiO}_2$  matrix does not modify the UV-absorption threshold of  $\text{TiO}_2$  [17]. This confirms the results of our TEM investigation, which indicated that the crystalline lattice of  $\text{TiO}_2$  remains unchanged after the synthesis [7].

Supplementary Fig. S5 related to this article can be found, in the online version, at <http://dx.doi.org/10.1016/j.apcatb.2014.10.002>.

When Ag is included in our photocatalysts, their absorption behavior is significantly changed. Specifically, a notable absorption in the region corresponding to visible light (more than 400 nm) can be observed. The previously reported absorption at visible wavelengths in our sols (Fig. 1) is also present in the photocatalysts (Fig. 5). This can be once more time attributed to the LSPR absorption of Ag nanoparticles [9].

Regarding the increase in Ag loadings in our photocatalysts, we observe (1) a very good correspondence between the increase of the Ag loadings and the decrease of the band-gap of our photocatalysts (Table 1), (2) that a slight blue-shift of the maximum absorption at visible wavelengths of the nanocomposites containing Ag is produced (Fig. 5). We speculate that this blue-shift may be due to a modification of the collective absorption behavior of Ag nanoparticles, which favors the interaction between individual nanoparticles. Our TEM discussion corroborates this hypothesis because Ag nanoparticles at S1T10Ag present the best dispersion and the smaller size among all the photocatalysts, therefore, enhancing the previously described absorption behavior. Xiao et al. [8] have previously reported that this blue-shift could be beneficial to enhance the photodegradation of methylene blue because the absorption peak produced by Ag nanoparticles shows an improved matching with the energy band gap of  $\text{TiO}_2$ .

The  $^{29}\text{Si}$  NMR spectra for all the nanocomposites obtained are shown in Fig. 6. All of the materials under study show two peaks at chemical shifts of  $-100$  ppm and  $-110$  ppm corresponding, respectively, to Q3 and Q4 structural units. In all these materials, except for materials with higher  $\text{TiO}_2$  and Ag loading (S1T10Ag, S4T1Ag and S4T5Ag), the Q4 peak, attributable to tetrafunctional build-ups, is higher than that corresponding to Q3, indicating a more cross-linked framework due the effect of *n*-octylamine. This higher degree of reticulation is typical of silica particle mesostructures obtained using amine surfactants as a template [39,43]. This finding confirms that *n*-octylamine produces nanomaterials composed



**Table 2**  
Properties of the treated stone specimens and the untreated counterparts.<sup>a</sup>

	Uptake (% w/w)	Dry matter (% w/w)	$\Delta E^*$	TWU (% w/w)	Material removed by peeling (mg)
UNT	–	–	–	2.03 ± 1.28	2.1 ± 0.2
S0T0Ag	0.49 ± 0.02	0.28 ± 0.02	3.78 ± 0.15	0.21 ± 0.15	0.6 ± 0.2
S1T0Ag	0.42 ± 0.05	0.28 ± 0.03	1.63 ± 0.04	0.05 ± 0.00	0.6 ± 0.1
S1T1Ag	0.49 ± 0.05	0.26 ± 0.01	3.18 ± 0.36	0.34 ± 0.36	0.4 ± 0.2
S1T5Ag	0.58 ± 0.09	0.26 ± 0.01	4.13 ± 0.59	0.35 ± 0.02	1.1 ± 0.3
S1T10Ag	0.34 ± 0.04	0.18 ± 0.02	4.76 ± 0.79	0.26 ± 0.08	1.3 ± 0.1
S4T0Ag	0.58 ± 0.06	0.35 ± 0.05	1.48 ± 0.10	0.10 ± 0.02	1.1 ± 0.2
S4T1Ag	0.64 ± 0.09	0.36 ± 0.09	1.86 ± 0.31	0.08 ± 0.05	0.4 ± 0.2
S4T5Ag	0.41 ± 0.04	0.20 ± 0.01	14.62 ± 0.41	–	–
S4T10Ag	n.g.	n.g.	–	–	–

<sup>a</sup> Data correspond to average values. Standard deviations are also included.

of a network of silica particles, as previously discussed our SEM discussion (Fig. 2). The lower intensity observed in Q4 for materials with higher TiO<sub>2</sub> and Ag loading indicates, a priori, that less reticulation is produced.

Other significant differences according to the TiO<sub>2</sub> and Ag content were also observed. In the case of TiO<sub>2</sub>–SiO<sub>2</sub> photocatalysts, the signals from Q1 and Q2 are either absent (S4T0Ag) or observed as a very weak signal (a Q2 peak is observed for S1T0Ag). Davis et al. [44] also observed an increase in signals corresponding to a reduced silica reticulation as TiO<sub>2</sub> content was raised.

When Ag loading is increased, more intense Q1 (–89 ppm) and Q2 (–91 ppm) signals and a decrease of Q3 and Q4 signals can be observed. This difference is due to an incomplete condensation of silica and consequently, some ethoxy groups are present in the material. This information is in good agreement with the increased aggregate size detected by SEM. Here, we can confirm that these larger aggregates are also less condensed silica structures. The absence of sol–gel transition verified for S4T10Ag is also an important indication of the same reduction in condensation rates for higher Ag loading values. This finding confirms the role played by the *n*-octylamine as catalyst during the sol–gel transition, and the inhibition of its catalytic action by the presence of Ag, previously discussed in this manuscript.

### 3.2. Application on stone, and characterization

The photocatalysts synthesized in this study were sprayed as sols, under laboratory conditions, onto a building limestone in order to investigate its photocatalytic behavior and adhesion to the stone. S0T0Ag was also evaluated for comparison purposes.

One of the most important practical limitations on the prospective employment of these photocatalysts as coatings would be encountered if they produced changes in the color of the treated stones. Therefore, total color difference values ( $\Delta E^*$ ) of the stone induced by the photocatalysts were measured and these results are given in Table 2. Nearly all the photocatalysts produced color changes close to the generally accepted threshold value ( $\Delta E^* \leq 5$ ), even for the most restrictive applications such as ancient building restoration [45]. S4T5Ag was the only photocatalyst presenting a color change value beyond the indicated threshold, probably due to the highest Ag loading included in its formulation. For this reason, this material was not considered for further investigation.

This parameter is critical for Ag–SiO<sub>2</sub>–TiO<sub>2</sub> materials. TiO<sub>2</sub> is widely used as a white pigment for its considerable hiding power and produces a visible whitening effect on stone samples. Ag contributes for the generation of darker nanocomposites. We confirmed that two important features of our application method contribute for reducing the color change to suitable values for application on stone surfaces and buildings. Firstly, by dispersing particles of sizes reduced to the nanoscale, these coatings

also reduce the hiding power of TiO<sub>2</sub> and Ag and minimize the possibilities of significant color change. Secondly, we remove the excess of sol on the stone surface directly after its application.

Uptake and dry matter of the sols under study are shown in Table 2. Although some variations were found between samples due the heterogeneity of the limestone samples, we observe certain trends, as follows: the sols with higher Ag loading in their corresponding series (S1T10Ag and S4T5Ag) produce the lowest uptake and dry matter among the sols applied. This trends are explained because the higher Ag nanoparticles content generates a suppressive effect of *n*-octylamine as a sol–gel catalyst and a decrease in the condensation rate, as we previously discussed in the previous paragraphs of this paper. Thus more sol could evaporate during the application of the sol and generate lower dry matter values.

Since one significant drawback of commercial products applied on stone has been the reduced photocatalytic efficiency found during long-term use, due to the elimination of TiO<sub>2</sub> from the stone surface [12], we have performing a peeling test adapted from the literature [27], in order to investigate the degree of adhesion of the coatings applied on stone. Table 2 shows the weight lost by the untreated stone and its treated counterparts after testing.

The greatest loss of mass after the peeling test is observed for the untreated stone (see Table 2). The untreated stone surface presents a considerable amount of loose matter which can easily be detached through our adhesion testing method. Stone samples treated with S1T0Ag and S1T1Ag show almost negligible loss of mass (see Table 2). These findings confirm that TiO<sub>2</sub> and Ag have been integrated into the SiO<sub>2</sub> matrix, which has, in turn, adhered firmly to the stone. In this respect, the inclusion of the photocatalyst in a mesoporous silica coating is an interesting solution for keeping particles well adhered to the surface, to provide long-term wear resistance.

The test removed a slightly larger amount of material from the stone surface, for higher TiO<sub>2</sub> and Ag nanoparticles content, reaching a maximum for the S1T5Ag, S1T10Ag and S4T1Ag coatings. We associate this result with the formation of a less condensed SiO<sub>2</sub> matrix, as was previously confirmed through <sup>29</sup>Si NMR.

In order to evaluate the ability of the nanocomposites to prevent penetration of water into the stone, we have carried out a capillary water absorption test. Total water uptake (TWU) values obtained after 48 h are shown in Table 2. The results confirm that our nanocomposites effectively prevent the penetration of water into the stone pores, since the uptake values obtained for all the treated samples is close to zero and significantly lower than the value those obtained for the untreated counterpart. It is also important to remark that this decrease in water absorption is more related with a pore-filling effect than with a highly hydrophobic behavior induced by the treatments, which could contribute for the reduction of the presence of OH• free radicals on the surface of the photoactive coatings.



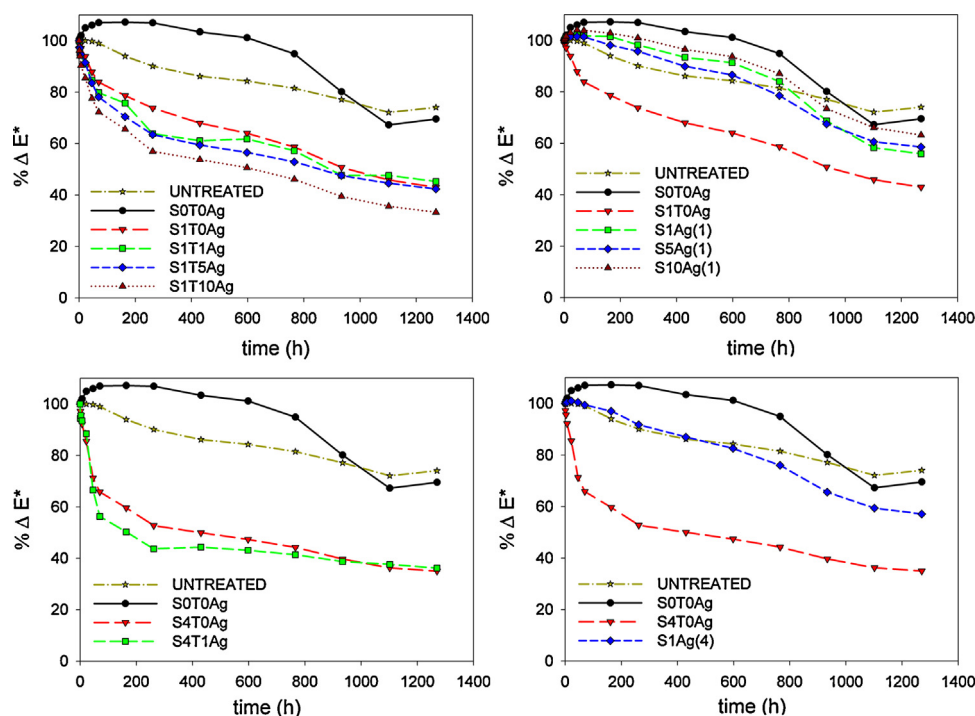


**Fig. 7.** Evolution of  $\% \Delta E^*$  (for methylene blue stains) on treated and untreated samples of limestone. The samples were previously stained with methylene blue (MB) and then irradiated with UV light ( $\lambda_{\min} = 365$  nm) for more than 1000 h.

Finally, and most importantly, we have investigated the self-cleaning properties of the photocatalysts synthesized in our laboratory and applied to the limestone tested, by carrying out a photo-degradation test of stains deposited previously on the stone surface. Methylene blue (MB) was used as the staining agent, dissolved in ethanol in order to ensure rapid evaporation of all the liquid. The evolution of total color differences ( $\Delta E^*$ ) under UV light, with the time was recorded, and results are shown in Fig. 7, for the photocatalysts under study. Limestones treated with S and S<sub>Ag</sub>(#) coatings and untreated samples were included in this test for comparison purposes. The photocatalytic activity is expressed as  $\% \Delta E^*$ , which is given by the following expression:  $100 - (((\Delta E^* - \Delta E^*_0) / \Delta E^*_0) \times 100)$ , where  $\Delta E^*_0$  is the value obtained for the total color difference between the stained and unstained samples at the beginning of the test ( $t = 0$  h).  $\Delta E^*$  corresponds to the same measurements recorded at each irradiation time.

The conditions of this test make the following comments relevant: (1) it was performed in the absence of liquid water and with around 30% relative humidity (RH) values; therefore, degradation times are necessarily slower than in experiments carried out in high moisture, because the generation of  $\text{OH}^\bullet$  free radicals is lower than if these products are applied on buildings outdoors with higher RH values; (2) our test has been carried out in the presence of atmospheric oxygen and at neutral pH conditions, thus ensuring that all the color variations are due to the elimination of MB, and not to the undesirable formation of the leuco form of MB (LMB) [46]; (3) we have evaluated photodegradation by measuring the total color variation parameter because it very useful for testing the degradation, in situ, for portable color measurements.

Regarding the results obtained (see Fig. 7), the final  $\% \Delta E^*$  value reached for the untreated stone is 75% of the initial  $\Delta E^*$  value, corresponding to the degradation of MB due to purely photochemical mechanisms [46]. The degradation profiles obtained for S (containing  $\text{SiO}_2$ ), S<sub>Ag</sub>(1) and S<sub>Ag</sub>(4) (containing Ag and  $\text{SiO}_2$ ) show similar tendencies due to the same mechanisms observed for the

untreated sample. The slight differences in the MB degradation profiles that can be observed between the materials are not due to photocatalytic mechanisms.

In the case of the limestone samples treated with the photocatalyst coatings, from the profiles two different rates of degradation at different times can be clearly distinguished. Very rapid MB bleaching occurs in the first 72 h. Next, slower degradation rates are observed over the longer term. As we reported previously [18], we think the photocatalytic action of the nanocomposites produces most of the total degradation effect on the stain in the first few hours of exposure (the first part of the curve). We speculate that the second stage, with a much slower rate of degradation, may be caused by an effect of recalcitrant products of the degradation of pollutants substances that slowly contribute to the deactivation of the photocatalyst [47].

We have previously observed that an increase in the  $\text{TiO}_2$  content from 1% to 4% produced an enhancement of the photoactivity on stone due to the faster degradation of MB in the first 72 h verified for S4T0Ag [17]. This previous result is now confirmed for the type of stone tested in this paper.

A comparison of the four nanocomposites loaded to 1% with  $\text{TiO}_2$  and increasing Ag loadings reveals clear differences in the photoactivity. Specifically, S1T<sub>Ag</sub> materials present increasing slopes for higher Ag loadings in the first part of the curve. Therefore, the photoactivity of this series of nanomaterials could be organized in the following order: S1T10Ag > S1T5Ag > S1T1Ag > S1T0Ag. At the end of the test, it is also clear that S1T10Ag was able to degrade more MB than all the other photocatalysts. Similar increases in the photoactivity for higher Ag loading were observed by Liu et al. [7].

The improved textural parameters, such as surface area and pore volume (see Table 1 and Fig. 3), could be responsible for the increased photoactivity observed. We [18] and other authors [48] have previously reported that the photocatalytic degradation of MB is clearly enhanced by the addition of  $\text{TiO}_2$  particles to a  $\text{SiO}_2$  mesoporous structure, in contrast with the weaker effect observed when the particles are integrated in a dense microporous matrix.

The improved visible light absorption seems also to contribute for the better activity of S1T10Ag with respect to all the other photocatalysts in its series. It seems that a smaller average size and better dispersion of Ag nanoparticles present in S1T10Ag coatings, as observed by TEM/STEM, is more able to improve the photoactivity. Our TEM investigation also shows that a thin SiO<sub>2</sub> interlayer exists between TiO<sub>2</sub> and Ag nanoparticles integrated in our nanocomposites. By improving the dispersion of Ag nanoparticles, we assume that the thickness of the SiO<sub>2</sub> interlayer between TiO<sub>2</sub> and Ag is also reduced, because Ag nanoparticles are situated closer to TiO<sub>2</sub> (Fig. 4). This results in a better tuning of the LSPR of Ag nanoparticles and generates a better matching with the energy band-gap of TiO<sub>2</sub>, as Kumar et al. [3] and Jiang et al. [9] previously described.

The comparison of the two nanocomposites loaded with 4% TiO<sub>2</sub> also reveals differences in their photoactivity. In this case, as we previously described, high Ag loadings have inhibited the sol–gel transition (S4T10Ag) and have generated a color change that is higher the human perception threshold. Therefore, only one photocatalyst belonging to this series could be tested in the degradation of MB stains. In this case, we have observed an improvement of the photoactivity for S4T1Ag with respect to S4T0Ag. This can be attributed to the coarsening of the pore network and to the enhancement of the visible light absorption corresponding to the Ag-loaded nanocomposite (see Table 1; Figs. 3 and 5).

From the results discussed above, we can conclude that the mesostructure of the photocatalyst, created by *n*-octylamine, plays an important role in the photocatalytic activity of the materials under study. The surfactants also contribute for reducing Ag species in the sols and for the improving the stability of the dispersions of TiO<sub>2</sub> and Ag nanoparticles during the sol–gel transition. The activity of our photocatalysts is also enhanced because due to the presence of mesopores, which contribute to improving surface area, and pore volume of our materials and assist rapid MB diffusion toward the photoactive sites [18].

In addition, several synergistic effects occur with the SiO<sub>2</sub> matrix: (1) it acts as an absorber and provides access to the TiO<sub>2</sub> photocatalytic sites, (2) it generates an interlayer between TiO<sub>2</sub> and Ag nanoparticles, and contributes for tuning the LSPR of Ag nanoparticles with the energy bandgap of TiO<sub>2</sub>.

#### 4. Conclusions

We have designed an innovative synthesis route for producing Ag–SiO<sub>2</sub>–TiO<sub>2</sub> photocatalysts with application as self-cleaning and decontaminating coatings on stones and other building materials. Our route consists of mixing a silica oligomer, titania particles, a silver source and a surfactant. In this synthesis, the surfactant constituent acts: (1) to disperse the TiO<sub>2</sub> and Ag particles; (2) to contribute for the reduction of Ag<sup>+</sup> ions to Ag, (3) to catalyze the sol–gel transition and (4) to coarsen the porous gel network, thus providing better access to photoactive sites.

From our in-depth investigation of the light absorption and of the texture of these photocatalysts, we conclude that they are both key parameters for the increase of the photocatalytic activity. Specifically, we find that the integration of higher Ag loadings in a TiO<sub>2</sub>–SiO<sub>2</sub> network (10% w/w) significantly increase the photoactivity of the coating containing 1% (w/v) TiO<sub>2</sub> due to the improved absorption of visible light and higher surface area of the photocatalyst. For higher TiO<sub>2</sub> contents (4% w/v) there is an increase in photoactivity for 1% (w/w) Ag loading. Higher Ag loadings (5% w/w) generate an undesired color change on stone or inhibit the sol–gel transition of the coatings (10% w/w).

Finally, we believe that the photocatalysts synthesized have clear practical applications, because the products obtained by this

route can be applied externally, outdoors, in a simple and low-cost process, producing coatings, which adhere firmly to the stone and preserve the esthetic qualities of the stone.

#### Acknowledgments

We are grateful for financial support from the Spanish Government/FEDER-EU (MAT2013-42934-R and Project Geopetra, Innopacto subprogram), and the Government of Andalusia (project TEP-6386 and Group TEP-243). We also thank Prof. Jesús Ayuso (University of Cádiz), Prof. Aurelio Cabeza and SCAI (University of Málaga) for their help and fruitful discussion of UV–vis spectra.

#### References

- [1] J. Chen, C. Poon, *Build. Environ.* 44 (2009) 1899.
- [2] M. Peláez, N.T. Nolan, S.C. Pillai, M.K. Seery, P. Falaras, A.G. Kontos, P.S.M. Dunlop, J.W.J. Hamilton, J.A. Byrne, K. O'Shea, M.H. Entezari, D.D. Dionysiou, *Appl. Catal. B: Environ.* 125 (2012) 331.
- [3] M.K. Kumar, S. Krishnamoorthy, L.K. Tan, S.Y. Chiam, S. Tripathy, H. Gao, *ACS Catal.* 1 (2011) 300.
- [4] K. Awazu, M. Fujimaki, C. Rockstuhl, J. Tominaga, H. Murakami, Y. Ohki, N. Yoshida, T. Watanabe, *J. Am. Chem. Soc.* 130 (2008) 5.
- [5] Q. Chen, H. Shi, W. Shi, Y. Xu, D. Xu, *Catal. Sci. Technol.* 2 (2012) 1213.
- [6] Y. Horiuchi, M. Shimada, T. Kamegawa, K. Mori, H. Yamashita, *J. Mater. Chem.* 19 (2009) 6745.
- [7] C. Liu, D. Yang, Y. Jiao, Y. Tian, Y. Wang, Z. Jiang, *Appl. Mater. Interfaces* 5 (2013) 3824–3832.
- [8] J. Xu, X. Xiao, A. Stepanov, F. Ren, W. Wu, G. Cai, S. Zhang, Z. Dai, F. Mei, C. Jiang, *Nanoscale Res. Lett.* 8 (2013) 73.
- [9] J. Zhou, F. Ren, S. Zhang, W. Wu, X. Xiao, Y. Liu, C. Jiang, *J. Mater. Chem. A* 1 (2013) 13128–13138.
- [10] S.D. Standridge, G.C. Schatz, T.H. Joseph, *Langmuir* 25 (2009) 2596.
- [11] L. Bergamonti, I. Alfieri, M. Franzò, A. Lorenzi, A. Montenero, G. Predieri, M. Raganto, A. Calia, L. Lazzarini, D. Bersani, P.P. Lottici, *Environ. Sci. Pollut. Res.* (2013), <http://dx.doi.org/10.1007/s11356-013-2136-5>.
- [12] P. Munafò, E. Quagliarini, F. Bondioli, G.B. Goffredo, F. Bondioli, A. Liciulli, *Constr. Build. Mater.* 65 (2014) 218.
- [13] M.F. La Russa, S.A. Ruffolo, N. Rovella, C.M. Belfiore, A.M. Palermo, M.T. Guzzi, G.M. Crisci, *Progr. Org. Coat.* 74 (2012) 186.
- [14] K. Rao, M. Subrahmanyam, P. Boule, *Appl. Catal. B: Environ.* 49 (2004) 239.
- [15] P. Krishnan, M. Zhang, Y. Cheng, D.T. Riang, L.E. Yu, *Constr. Build. Mater.* 43 (2013) 197.
- [16] J. Macmullen, J. Radulovic, Z. Zhang, H.N. Dhakal, L. Daniels, J. Elford, M.A. Leost, N. Bennet, *Constr. Build. Mater.* 49 (2013) 93.
- [17] L. Pinho, M.J. Mosquera, *Appl. Catal. B: Environ.* 205 (2013) 134–135.
- [18] L. Pinho, M.J. Mosquera, *J. Phys. Chem. C* 115 (2011) 22851.
- [19] D. Facio, M.J. Mosquera, *Appl. Mater. Interfaces* 5 (2013) 7517.
- [20] J.F. Illescas, M.J. Mosquera, *J. Phys. Chem. C* 115 (2011) 14624.
- [21] M.J. Mosquera, A. Montes, D.M. de los Santos, US Patent US 11/997,365.
- [22] M.J. Mosquera, L. Pinho, Spanish Patent P201100741, Priority date: June 24th 2011.
- [23] M. Thommes, B. Smarsly, M. Groenwolt, P.I. Ravikovitch, A.V. Neimark, *Langmuir* 22 (2006) 756.
- [24] J.M. Thomas, P.A. Midgley, T.J.V. Yates, J.S. Barnard, R. Raja, I. Arslan, M. Weyland, *Angew. Chem. Int. Ed.* 43 (2004) 6745.
- [25] S.P. Tandon, J.P. Gupta, *Phys. Stat. Sol.* 38 (1970) 363.
- [26] A.P. Ferreira Pinto, J. Delgado Rodrigues, *J. Cultural Herit.* 9 (2008) 38.
- [27] M. Drdácák, J. Lesák, S. Rescic, Z. Slížková, P. Tiano, J. Valach, *Mater. Struct.* 45 (2012) 505.
- [28] UNE-EN 1925, Natural Stone test methods. Determination of water absorption coefficient by capillarity, AENOR, 1999.
- [29] R.S. Berns, Billmeyer and Saltzman's Principles of Color Technology, Wiley-Interscience, New York, 2000.
- [30] ISO 10678, Fine ceramics (advanced ceramics, advanced technical ceramics); determination of photocatalytic activity of surfaces in an aqueous medium by degradation of methylene blue, ISO, 2010.
- [31] L. Pinho, F. Elhaddad, D.S. Facio, M.J. Mosquera, *Appl. Surf. Sci.* 275 (2013) 389.
- [32] X. Wu, X. Yao, M. Wang, L. Gao, *Ceram. Int.* 30 (2004) 1949.
- [33] Y. Kobayashi, H. Katakami, E. Mine, D. Nagao, M. Konno, L. Liz-Marzán, *J. Colloid Interface Sci.* 283 (2005) 392.
- [34] A. Frattini, N. Pellegrini, D. Nicastro, O. de Sanctis, *Mater. Chem. Phys.* 94 (2005) 148.
- [35] H. Hiramatsu, F.E. Osterloh, *Chem. Mater.* 16 (2004) 2509.
- [36] M.C. Hidalgo, M. Maicu, J.A. Navío, G. Colón, *Appl. Catal. B: Environ.* 81 (2008) 49.
- [37] K. Kosuge, P.S. Singh, *Microporous Mesoporous Mater.* 44–45 (2001) 139.
- [38] G.H. Bogush, C.F. Zukoski, *J. Colloid Interface Sci.* 142 (1991) 19.
- [39] J.F. Illescas, M.J. Mosquera, *ACS Appl. Mater. Interfaces* 4 (2012) 4259.

- [40] E. Beyers, P. Cool, E. Vansant, J. Phys. Chem. B 109 (2005) 10081.
- [41] M. Kruk, M. Jaroniec, Chem. Mater. 13 (2001) 3169.
- [42] B. Llano, G. Restrepo, J.M. Marín, J.A. Navío, M.C. Hidalgo, Appl. Catal. B: Environ. 387 (2010) 135.
- [43] P.T. Tanev, T. Pinnavaia, Chem. Mater. 8 (1996) 2068.
- [44] R. Davis, Z. Liu, Chem. Mater. 9 (1997) 2311.
- [45] C. Miliari, M.L. Velo-Simpson, G.W. Scherer, J. Cult. Herit. 8 (2007) 1.
- [46] A. Mills, J. Wang, J. Photochem. Photobiol. A: Chem. 127 (1999) 123.
- [47] A. Mills, C. Hill, P.K.J. Robertson, J. Photochem. Photobiol. A 237 (2012) 7.
- [48] N. Suzuki, X. Jiang, L. Radhakrishnan, K. Takai, K. Shimasaki, Y. Huang, N. Miyamoto, Y. Yamauchi, Bull. Chem. Soc. Jpn. 84 (2011) 812.